

Cite this: *J. Mater. Chem.*, 2012, **22**, 20566

www.rsc.org/materials

PAPER

Facile synthesis of single-crystalline mesoporous  $\alpha$ -Fe<sub>2</sub>O<sub>3</sub> and Fe<sub>3</sub>O<sub>4</sub> nanorods as anode materials for lithium-ion batteries†Zhen Xiao,<sup>a</sup> Yang Xia,<sup>b</sup> Zhaohui Ren,<sup>\*a</sup> Zhenya Liu,<sup>a</sup> Gang Xu,<sup>a</sup> Chunying Chao,<sup>a</sup> Xiang Li,<sup>a</sup> Ge Shen<sup>a</sup> and Gaorong Han<sup>\*a</sup>

Received 24th June 2012, Accepted 14th August 2012

DOI: 10.1039/c2jm34083f

In this work, single-crystalline  $\alpha$ -FeOOH nanorods with a length of 400–700 nm and a diameter of 20–80 nm were successfully synthesized *via* a facile template-free hydrothermal method. Single-crystalline mesoporous  $\alpha$ -Fe<sub>2</sub>O<sub>3</sub> and Fe<sub>3</sub>O<sub>4</sub> nanorods could be obtained from these  $\alpha$ -FeOOH precursors after calcining at 350 °C in air and 500 °C in nitrogen, respectively. The as-prepared single-crystalline mesoporous  $\alpha$ -Fe<sub>2</sub>O<sub>3</sub> and Fe<sub>3</sub>O<sub>4</sub> nanorods exhibited a large specific surface area and porosity, effectively enhancing the electrochemical reaction area and accommodate the strain during the charge–discharge cycling process.

## 1. Introduction

One-dimensional (1D) nanomaterials, such as nanorods, nanobelts, nanotubes and nanowires,<sup>1–6</sup> have been the focus of much attention because of their improved chemical and physical performances over solid materials, as well as their intriguing applications in nanoreactors, catalysis,<sup>7,8</sup> drug delivery<sup>1,6</sup> and energy storage for renewable energy sources.<sup>4,9</sup> Lithium-ion batteries (LIBs) are regarded as the most promising rechargeable energy storage technology for the rapid depletion of fossil fuels and the increasing applications of portable electronic devices and transportation. In order to meet the requirements of high power and energy density, 3d-transition-metal binary compounds (such as Fe<sub>2</sub>O<sub>3</sub>,<sup>10–12</sup> Fe<sub>3</sub>O<sub>4</sub>,<sup>13–15</sup> Co<sub>3</sub>O<sub>4</sub>,<sup>4,16</sup> NiO<sup>17–19</sup> and SnO<sub>2</sub>,<sup>9,20</sup> *etc.*) with various nanostructures have been extensively explored as LIB anode materials due to their unique characteristics. In this field, binary iron oxides such as  $\alpha$ -Fe<sub>2</sub>O<sub>3</sub> and Fe<sub>3</sub>O<sub>4</sub> are believed to be the most promising electrode materials for energy storage, due to their low cost, environmentally friendly nature and fascinating properties.<sup>21,22</sup> Moreover, both of them have high theoretical capacities, 1004 mA h g<sup>−1</sup> for  $\alpha$ -Fe<sub>2</sub>O<sub>3</sub> and 924 mA h g<sup>−1</sup> for Fe<sub>3</sub>O<sub>4</sub>, respectively.<sup>23</sup> Therefore, LIBs based on  $\alpha$ -Fe<sub>2</sub>O<sub>3</sub> and Fe<sub>3</sub>O<sub>4</sub> nanostructures have been widely investigated over the past decades.<sup>2,10,11,21,24,25</sup>

It has been demonstrated that the specific capacity and cycling performance of  $\alpha$ -Fe<sub>2</sub>O<sub>3</sub> and Fe<sub>3</sub>O<sub>4</sub> electrodes are strongly associated with their morphologies and microstructures.<sup>20,24–26</sup> In particular, binary iron oxide nanostructures with a dense porosity and large surface area could effectively shorten the diffusion pathway of lithium ions and electrons, and increase the electrochemical reaction area, allowing the improved penetration of electrolyte and accommodating the strain of Li insertion–extraction. For example, Zhou *et al.* have synthesized hierarchical mesoporous hematite by heating the iron oxyhydroxide precursor, where high specific surface area and rich mesoporosity enhanced the conductivity of electrons, as well as favoring the transfer and storage of lithium ions.<sup>26</sup> Chen *et al.* reported a facile top-down approach to fabricate porous  $\alpha$ -Fe<sub>2</sub>O<sub>3</sub> melon-like microparticles with significantly improved capacity retention.<sup>21</sup> At present, various methods have been employed to synthesize porous iron oxides, such as the electrospinning technique,<sup>10</sup> template preparation,<sup>8</sup> the solid-state thermal annealing method,<sup>26</sup> hydrothermal synthesis,<sup>11</sup> a top-down approach<sup>21</sup> and so on. However, a facile and low cost approach to the synthesis of 1D single-crystalline  $\alpha$ -Fe<sub>2</sub>O<sub>3</sub> and Fe<sub>3</sub>O<sub>4</sub> with porous structures remains unavailable.

In this work, we developed a facile route by using  $\alpha$ -FeOOH as a precursor to fabricate single-crystalline mesoporous  $\alpha$ -Fe<sub>2</sub>O<sub>3</sub> and Fe<sub>3</sub>O<sub>4</sub> nanorods. Owing to the high surface area and porosity of the as-obtained  $\alpha$ -Fe<sub>2</sub>O<sub>3</sub> and Fe<sub>3</sub>O<sub>4</sub> nanorods, the corresponding electrode material exhibits a high reversible capacity, and remarkable rate and cycling performance.

## 2. Experimental

In this work, all chemicals are reagent grade and were used without further purification. The main process of synthesizing

<sup>a</sup>State Key Laboratory of Silicon Materials, Department of Materials Science and Engineering, Cyrus Tang Center for Sensor Materials and Applications, Zhejiang University, Hangzhou 310027, P.R. China. E-mail: renzh@zju.edu.cn; hgr@zju.edu.cn; Fax: +86-571-87952341; Tel: +86-571-87952341

<sup>b</sup>College of Chemical Engineering and Materials Science, Zhejiang University of Technology, Hangzhou, 310014, P. R. China

† Electronic supplementary information (ESI) available. See DOI: 10.1039/c2jm34083f

single-crystalline mesoporous  $\alpha$ -Fe<sub>2</sub>O<sub>3</sub> and Fe<sub>3</sub>O<sub>4</sub> nanorods was illustrated in a schematic picture (Scheme 1).

### 2.1. Synthesis of $\alpha$ -FeOOH nanorods

In a typical synthesis procedure, Fe(NO<sub>3</sub>)<sub>3</sub>·9H<sub>2</sub>O and KOH were used as the starting materials. The  $\alpha$ -FeOOH nanorods were synthesized *via* a hydrothermal method as follows: firstly, 0.01 mol Fe(NO<sub>3</sub>)<sub>3</sub>·9H<sub>2</sub>O and 0.04 mol KOH were each dissolved in 10 ml distilled water. Then, the KOH solution was dropped slowly into the Fe(NO<sub>3</sub>)<sub>3</sub>·9H<sub>2</sub>O solution under vigorous stirring. The suspension solution was poured into a stainless-steel Teflon-lined autoclave for the hydrothermal treatment, which was then filled with distilled water up to 80% of the total volume. The autoclave was sealed and maintained at 100 °C for 6 h. Finally, the autoclave was cooled to room temperature naturally, and the resulting solid products were filtered off, washed with absolute ethanol and distilled water several times, and then dried in an oven at 60 °C for 12 h.

### 2.2. Synthesis of single-crystalline mesoporous $\alpha$ -Fe<sub>2</sub>O<sub>3</sub> nanorods

In order to obtain mesoporous  $\alpha$ -Fe<sub>2</sub>O<sub>3</sub> nanorods, the as-prepared  $\alpha$ -FeOOH nanorod precursor was placed in an alumina crucible, and calcined at 350 °C for 30 min in air. After cooling down, the  $\alpha$ -FeOOH nanorod precursor changed from yellow to red, which meant that  $\alpha$ -FeOOH nanorods have transformed into  $\alpha$ -Fe<sub>2</sub>O<sub>3</sub> nanorods.

### 2.3. Synthesis of single-crystalline mesoporous Fe<sub>3</sub>O<sub>4</sub> nanorods

The single-crystalline mesoporous Fe<sub>3</sub>O<sub>4</sub> nanorods were prepared by the following procedure. 0.2 g  $\alpha$ -FeOOH nanorod precursor was placed inside an alumina boat. 2 ml of 10 wt% polystyrene (PS) suspended in dimethylformamide (DMF) was dropped onto the above  $\alpha$ -FeOOH nanorods. Then the  $\alpha$ -FeOOH–PS–DMF mixture was transferred into a tube furnace and heated at 500 °C for 2 h under a flowing nitrogen (N<sub>2</sub>) atmosphere.

### 2.4. Fabrication of electrode

The electrochemical performance of the samples was evaluated using CR2025 coin-type cells assembled in a glove box under an argon atmosphere. The working electrode was fabricated by

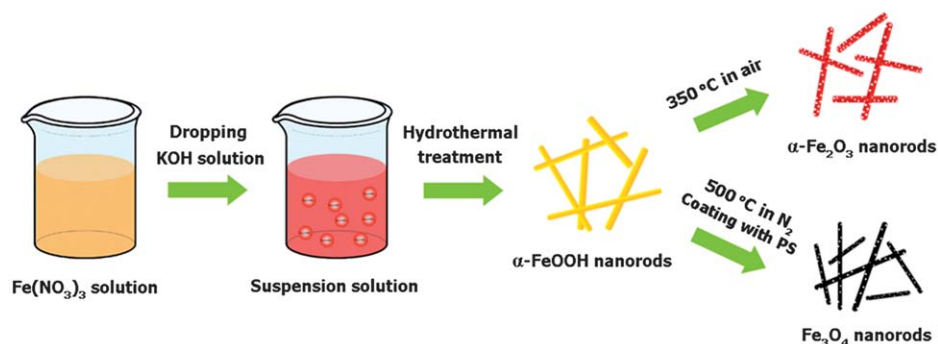
mixing the active material ( $\alpha$ -FeOOH,  $\alpha$ -Fe<sub>2</sub>O<sub>3</sub> and Fe<sub>3</sub>O<sub>4</sub>), acetylene black and polyvinylidene fluoride (PVDF) binder in the weight ratio of 6 : 2 : 2. A lithium foil was used as both the counter electrode and reference electrode. A 1 M solution of LiPF<sub>6</sub> in ethylene carbonate (EC)–dimethyl carbonate (DME) (1 : 1 in volume) was used as the electrolyte with a Celgard membrane as the separator.

### 2.5. Characterization

X-Ray powder diffraction patterns (XRD) were collected at room temperature on a Thermo ARL X'TRA powder diffractometer with Bragg–Brentano geometry by Cu K $\alpha$  radiation ( $\lambda$  = 1.54056 Å) under 0.82 Å resolution. The microstructural characteristics were studied using a field emission scanning electron microscope (SEM, Hitachi MODEL S-4800). Transmission electron microscope (TEM) images, and HRTEM images were taken *via* a transmission electron microscope (FEI, Tecnai G<sup>2</sup> F30) equipped with an EDS detector, using an accelerating voltage of 200 kV (with a double-tilt holder). The thermal analyses were determined by a SDT Q600 (TA Instruments, U.S.A) under air atmosphere and N<sub>2</sub> atmosphere at a heating rate of 10 °C min<sup>−1</sup> from room temperature to 700 °C. Nitrogen adsorption–desorption was determined by Brunauer–Emmett–Teller (BET) tests using ASAP 2020 (Micromeritics Instruments) surface area and pore analyzers. Electrochemical capacity measurements were performed on a Neware battery test system with galvanostatic charge and discharge in the voltage range of 0.05–3.0 V at room temperature. Cyclic voltammogram (CV) tests were performed by a CHI650B electrochemical workstation (Chenhua, Shanghai, China). CV curves were examined in the voltage range of 0.05–3.0 V at a scan rate of 0.1 mV s<sup>−1</sup>. Electrochemical impedance spectroscopy (EIS) tests were carried out with the frequency ranging from 0.1 to 10<sup>6</sup> Hz at room temperature.

## 3. Results and discussion

All XRD diffraction peaks of the  $\alpha$ -FeOOH nanorod precursors synthesized hydrothermally in Fig. 1a can be indexed to the orthorhombic  $\alpha$ -FeOOH with lattice constants of  $a$  = 4.608 Å,  $b$  = 9.956 Å and  $c$  = 3.022 Å (JCPDS no. 29-0713). The strong and sharp diffraction peaks indicate the highly crystalline nature of the  $\alpha$ -FeOOH nanorods. The morphology of the as-synthesized precursor products was investigated by SEM and TEM.



**Scheme 1** Schematic representation of synthesis of single-crystalline mesoporous  $\alpha$ -Fe<sub>2</sub>O<sub>3</sub> nanorods and Fe<sub>3</sub>O<sub>4</sub> nanorods.

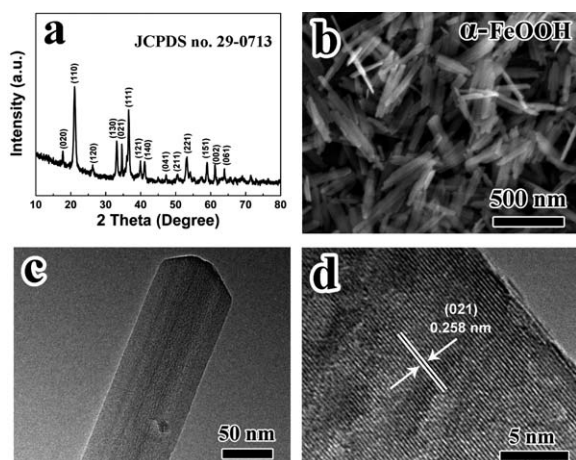


**Fig. 1** (a) XRD pattern of the as-prepared  $\alpha$ -FeOOH nanorods; (b) SEM image of the  $\alpha$ -FeOOH nanorods; (c) TEM image of an individual  $\alpha$ -FeOOH nanorod; (d) HRTEM image of an individual  $\alpha$ -FeOOH nanorod.

Fig. 1b and c show a low-magnification SEM image and a high-magnification TEM image of the obtained  $\alpha$ -FeOOH precursor with uniform 1D rod-like morphology, and their typical size is in the range of 20–80 nm in diameter and 400–700 nm in length (the detailed particle size distribution can be found in Fig. S1a and b†). The microstructure of the sample in Fig. 1d was further characterized by HRTEM. The relevant HRTEM image indicates a highly single-crystalline character with a distinct lattice spacing of 0.258 nm that corresponds to the value 0.258 nm of the (021) planes (JCPDS no. 29-0713).

Furthermore, thermogravimetric analysis and differential scanning calorimetry (TGA–DSC) measurements were performed to study the conversion process of the as-prepared  $\alpha$ -FeOOH during calcination in air and  $N_2$  atmosphere, respectively. Fig. 2a shows the thermal analysis process of the  $\alpha$ -FeOOH nanorods in air. From the TGA curve, the total weight loss is about 11.56%, which is slightly larger than the theoretical value (10.1%). In the range of room temperature to 250 °C, a 1.33% weight loss is attributed to adsorbed water molecules. The abrupt weight loss (~10.23%) that occurred in the range of 250–300 °C is due to the decomposition of  $\alpha$ -FeOOH precursors. Correspondingly, there are endothermic peaks in the DSC curve which may be ascribed to the removal of the structural water molecules and the crystallization process of  $\alpha$ -Fe<sub>2</sub>O<sub>3</sub>, respectively. After 300 °C, there was no change in the weight of the  $\alpha$ -FeOOH powders, suggesting that the  $\alpha$ -FeOOH sample

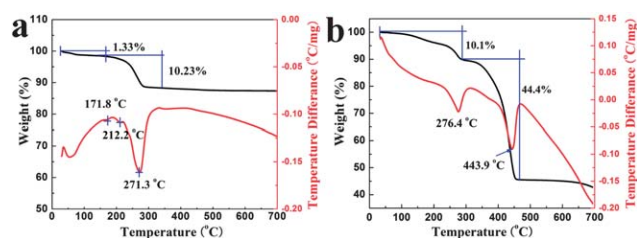


**Fig. 2** (a) TGA–DSC curves of  $\alpha$ -FeOOH nanorods in air atmosphere. (b) TGA–DSC curves of  $\alpha$ -FeOOH–PS mixture in  $N_2$  atmosphere.

was dehydrated completely and the stable residue can reasonably be ascribed to the pure  $\alpha$ -Fe<sub>2</sub>O<sub>3</sub> phase. Meanwhile, during the thermal analysis process of  $\alpha$ -FeOOH–PS under  $N_2$  atmosphere, there are two obvious weight loss processes in the TGA curve, as shown in Fig. 2b. Near 276.4 °C, there is a weight loss of about 10.1%, corresponding to an obvious endothermic peak in the DSC curve. This weight loss is attributed to the decomposition of the  $\alpha$ -FeOOH nanorods. In the range of 300 to 470 °C, another endothermic peak is situated at about 443.9 °C, where the weight of the sample experienced a drastic decrease (about 44.4%). This peak is possibly due to the combustion of the polymer that was used in the pre-treatment process.

Hence, single-crystalline mesoporous  $\alpha$ -Fe<sub>2</sub>O<sub>3</sub> nanorods have been prepared by the calcination of the  $\alpha$ -FeOOH precursors at 350 °C for 30 min in air. Fig. 3a presents an XRD pattern of the  $\alpha$ -Fe<sub>2</sub>O<sub>3</sub> nanorods. The diffraction peaks of the products were in agreement with those of the  $\alpha$ -Fe<sub>2</sub>O<sub>3</sub> phase (JCPDS no. 33-0664). No impurity peaks, such as  $\gamma$ -Fe<sub>2</sub>O<sub>3</sub> and Fe<sub>3</sub>O<sub>4</sub>, have been observed, indicating that the precursors were completely transformed into hematite at 350 °C. The morphology and size distribution of  $\alpha$ -Fe<sub>2</sub>O<sub>3</sub> were investigated by SEM (Fig. 3b and S1c and d†). The image clearly shows that the sample retains a rod-like morphology with an average diameter of about 20–80 nm and a length of about 320–680 nm. Compared to the smooth surface of the as-synthesized  $\alpha$ -FeOOH nanorods, it is interesting to find that the heat-treated sample has a mesoporous structure, as shown in the TEM image (Fig. 3c). Moreover, these pores open to the outer surface, and are almost isolated from each other. The corresponding statistical pore size distribution histogram (Fig. S2a†) obtained from the TEM image clearly shows the pore size is in the range of 1–8 nm, and most of them are around 3 nm. The formation of the pores is probably due to the removal of H<sub>2</sub>O from  $\alpha$ -FeOOH during the heating process. The HRTEM image of a typical  $\alpha$ -Fe<sub>2</sub>O<sub>3</sub> nanorod (Fig. 3d) shows a single-crystalline nature and regular lattice fringes with interplanar distances of 0.25 nm and 0.25 nm, which correspond to the (110) and (−120) planes, respectively.

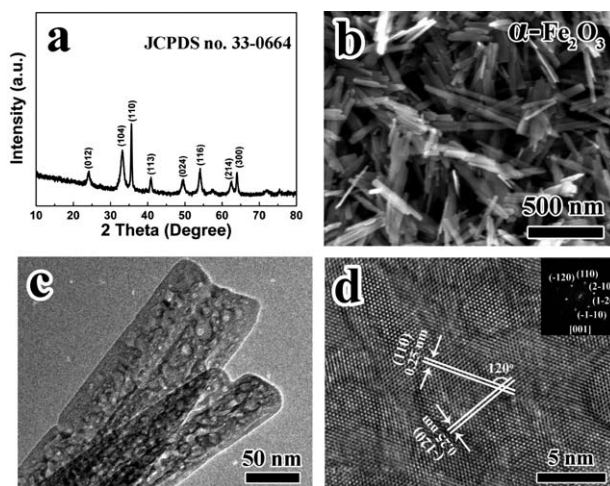


**Fig. 3** (a) XRD pattern of the as-prepared single-crystalline  $\alpha$ -Fe<sub>2</sub>O<sub>3</sub> nanorods; (b) SEM image of the  $\alpha$ -Fe<sub>2</sub>O<sub>3</sub> nanorods; (c) TEM image of an individual  $\alpha$ -Fe<sub>2</sub>O<sub>3</sub> nanorod; (d) HRTEM image of an individual  $\alpha$ -Fe<sub>2</sub>O<sub>3</sub> nanorod, the inset is the corresponding FFT image.



On the other hand, iron oxyhydroxide can be easily dehydrated into iron oxide, but the crystal phase varies, largely depending on the rearrangement of  $\text{Fe}^{3+}$  and  $\text{O}^{2-}$  ions. The single-crystalline mesoporous  $\text{Fe}_3\text{O}_4$  nanorods (JCPDS no. 19-0629) can be obtained easily by sintering the  $\alpha\text{-FeOOH}$  precursor in flowing  $\text{N}_2$  at  $500^\circ\text{C}$  for 2 h, which can be seen in Fig. 4a. The representative SEM image in Fig. 4b indicates the presence of large-scale 1D rod-like nanostructures with a rough surface, similar to the shape of the  $\alpha\text{-FeOOH}$  nanorods. The corresponding size distribution histograms (Fig. S1e and f†) of the  $\text{Fe}_3\text{O}_4$  nanorods reveal that the length of the nanorods is 300–700 nm and the diameter is 20–80 nm. The microstructure characterization was further investigated by TEM and HRTEM images, as shown in Fig. 4c and d. From Fig. 4c, the surface of the  $\text{Fe}_3\text{O}_4$  nanorods is mesoporous and coarse, consisting of dense nanopores with a size of 1–18 nm (Fig. S2b†). The HRTEM image (Fig. 4d) exhibits the single-crystalline character of the nanorod with a growth direction along the  $[-110]$ . The sharp diffraction spots of the corresponding indexed fast-Fourier-transform (FFT) pattern in the inset also verify that these  $\text{Fe}_3\text{O}_4$  nanorods are well crystallized.

The BET specific surface areas and porosity of  $\alpha\text{-FeOOH}$ ,  $\alpha\text{-Fe}_2\text{O}_3$  and  $\text{Fe}_3\text{O}_4$  nanorods were further studied by nitrogen adsorption–desorption analysis. As shown in Fig. 5a, c and e, the BET specific surface area of  $\alpha\text{-FeOOH}$ ,  $\alpha\text{-Fe}_2\text{O}_3$  and  $\text{Fe}_3\text{O}_4$  nanorods are 50.79, 88.07 and  $84.56\text{ m}^2\text{ g}^{-1}$ , respectively. It is apparent that the specific surface areas of the mesoporous  $\alpha\text{-Fe}_2\text{O}_3$  and  $\text{Fe}_3\text{O}_4$  samples are much larger than that of  $\alpha\text{-FeOOH}$  without a mesoporous structure, and the mesoporous  $\alpha\text{-Fe}_2\text{O}_3$  nanorods also have the largest specific surface area of  $88.07\text{ m}^2\text{ g}^{-1}$ . As shown in Fig. 5d–f, the pore size analysis, which is calculated from the desorption branches, demonstrates that the pore size distributions of  $\alpha\text{-Fe}_2\text{O}_3$  and  $\text{Fe}_3\text{O}_4$  are quite similar, and they both have a narrow pore size distribution of around 3 nm. After a careful comparison, a wide pore size distribution in the range of 20–120 nm can be found in each sample. In particular, it is very obvious for the  $\alpha\text{-FeOOH}$  sample (Fig. 5b). This

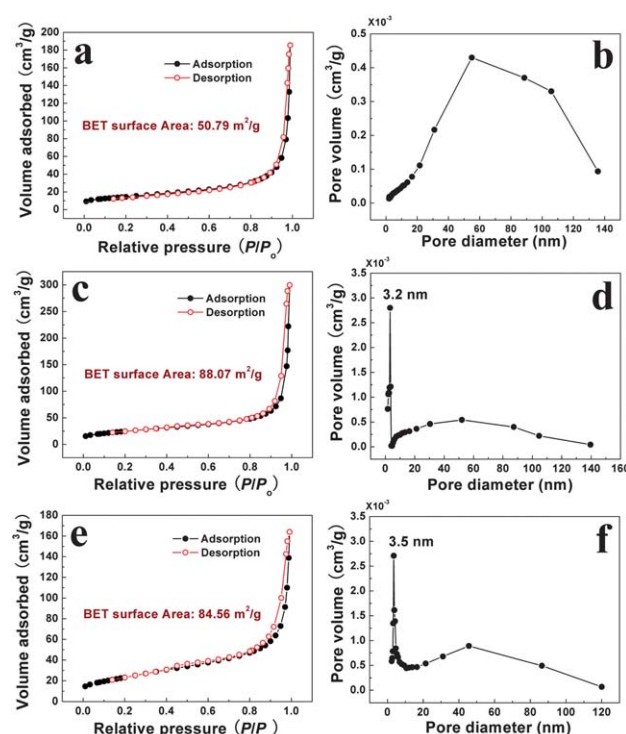


Fig. 5 Nitrogen adsorption–desorption isotherm loop and pore-size distribution curve calculated from the desorption branch by the BJH model. (a and b)  $\alpha\text{-FeOOH}$ ; (c and d)  $\alpha\text{-Fe}_2\text{O}_3$ ; (e and f)  $\text{Fe}_3\text{O}_4$ .

wide pore size distribution possibly originates from the interspaces between the packed nanorods. Therefore, it can be concluded that the high specific surface area of the  $\alpha\text{-Fe}_2\text{O}_3$  and  $\text{Fe}_3\text{O}_4$  nanorods arises from the mesoporous structure.

To evaluate the electrochemical performances of the  $\alpha\text{-FeOOH}$ ,  $\alpha\text{-Fe}_2\text{O}_3$  and  $\text{Fe}_3\text{O}_4$  nanorods, all the samples were

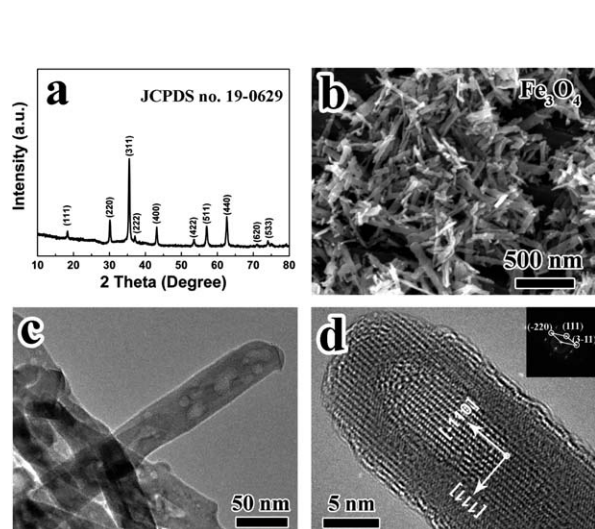


Fig. 4 (a) XRD pattern of the as-prepared single-crystalline  $\text{Fe}_3\text{O}_4$  nanorods; (b) SEM image of the  $\text{Fe}_3\text{O}_4$  nanorods; (c) TEM image of an individual  $\text{Fe}_3\text{O}_4$  nanorod; (d) the HRTEM image of an individual  $\text{Fe}_3\text{O}_4$  nanorod, the inset is the corresponding FFT image.

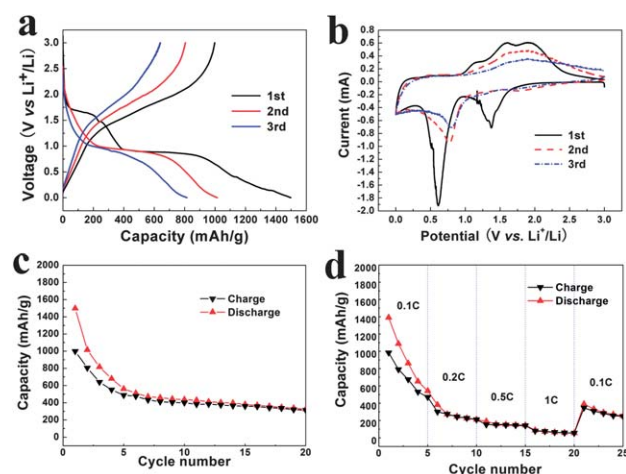
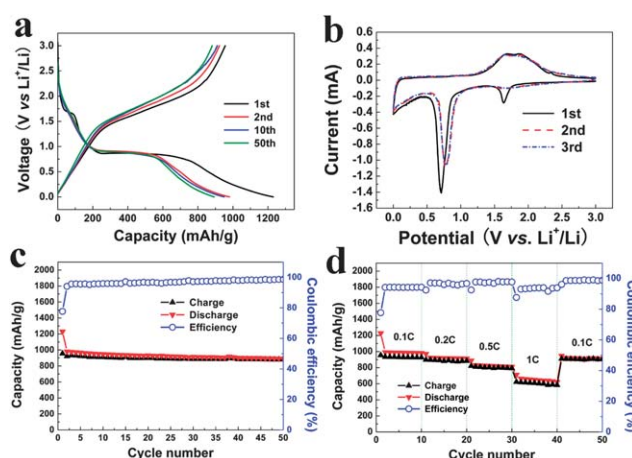


Fig. 6 (a) Charge–discharge profiles of single-crystalline  $\alpha\text{-FeOOH}$  nanorod electrodes at different cycles in the potential range from 0.05 to 3.0 V with a low current density of  $0.1\text{ C}$ ; (b) cyclic voltammogram curves of single-crystalline  $\alpha\text{-FeOOH}$  nanorod electrodes at a scan rate of  $0.1\text{ mV s}^{-1}$ ; (c) cycling performance of the cell at a  $0.1\text{ C}$  rate; (d) the rate performance of the single-crystalline  $\alpha\text{-FeOOH}$  nanorod electrode.

tested using CR2025 coin-type cells. As shown in Fig. 6a, there are two obvious voltage plateaus during the first discharge process of the  $\alpha$ -FeOOH sample. The long voltage plateau at 0.88 V corresponds to the reduction of  $\text{Fe}^{3+}$  to  $\text{Fe}^0$  ( $\alpha\text{-FeOOH} + 3\text{Li}^+ + 3\text{e}^- \leftrightarrow \text{Fe} + \text{LiOH} + \text{Li}_2\text{O}$ ).<sup>27</sup> The smaller plateau at 1.66 V can be attributed to lithium intercalation before the reduction reaction, since crystalline  $\alpha$ -FeOOH has a layered structure.<sup>28</sup> However, the smaller plateau located at 1.66 V could not be reproduced during the following charge–discharge processes, implying that this lithium intercalation process is irreversible. The first discharge and charge capacities are 1498.14 and 997.95  $\text{mA h g}^{-1}$  at a current density of 0.1 C (1 C = 905  $\text{mA g}^{-1}$ ), which has a low Coulombic efficiency of 66.6%. In addition, from the CV results (Fig. 6b), it could be found that there are two intense cathodic peaks at 0.61 and 1.38 V, which represent the conversion of  $\text{Fe}^{3+}/\text{Fe}^{2+}$  to  $\text{Fe}^0$  and lithium insertion into the crystal structure. Meanwhile, in the first anodic sweep, two small oxidation peaks at 1.62 and 1.94 V correspond to the oxidation of  $\text{Fe}^0$  to  $\text{Fe}^{2+}$  and  $\text{Fe}^{3+}$  to  $\text{Fe}_2\text{O}_3$ .<sup>27</sup> Nevertheless, in the subsequent cycles, the cathodic peak at 1.38 V disappears and two oxidation peaks are combined into one broad oxidation peak. The reproducibility of the CV curves after the second and third cycles is not as good. Furthermore, the inferior electrochemical performances of  $\alpha$ -FeOOH without a mesoporous structure also could be verified in long-term cycling (Fig. 6c) and multi-rate cycling tests (Fig. 6d). The  $\alpha$ -FeOOH electrode shows an initial discharge capacity of 1498  $\text{mA h g}^{-1}$  and decreases sharply to 324  $\text{mA h g}^{-1}$  at the 20<sup>th</sup> cycle under a low current density of 0.1 C, which is only 35.8% of the theoretical capacity (905  $\text{mA h g}^{-1}$ ). When the current density is increased from 0.1 to 1 C, the discharge–charge capacities decrease very fast. The discharge capacities of multi-rate cycling from 0.1 to 1 C are 542, 210, 145 and 54  $\text{mA h g}^{-1}$  at the end of each 5 cycles. Even though the current density reverses back to 0.1 C, the fast decay trend still continues. Based on the above results, it can be concluded that the lack of a mesoporous structure of the  $\alpha$ -FeOOH sample would not make it an ideal candidate for lithium storage.

According to previous reports, porous nanostructures have significant impact on the electrochemical properties. Yao *et al.* found that porous  $\alpha$ - $\text{Fe}_2\text{O}_3$  nanorods, compared to commercial ones, exhibited significantly enhanced cycling stability and rate capability due to their 1D porous structure.<sup>11</sup> Xiong *et al.* examined the electrochemical performance of porous  $\alpha$ - $\text{Fe}_2\text{O}_3$  microcubes and smooth  $\alpha$ - $\text{Fe}_2\text{O}_3$  microcubes.<sup>29</sup> The results clearly confirmed that porous  $\alpha$ - $\text{Fe}_2\text{O}_3$  microcubes were superior to smooth ones. Yuan *et al.* investigated mesoporous  $\text{Fe}_3\text{O}_4@\text{C}$  microcapsules and suggested that the mesopores played an important role in relieving the impact of volume changes during repeated charge–discharge processes.<sup>22</sup> Chen and his coworkers also investigated micro-sized porous  $\text{Fe}_3\text{O}_4$  particles and nano-sized solid  $\text{Fe}_3\text{O}_4$  particles.<sup>30</sup> Compared to the nano-sized solid  $\text{Fe}_3\text{O}_4$  sample, the micro-sized porous  $\text{Fe}_3\text{O}_4$  sample displayed good cycling performance and high capacity retention. Herein, the as-prepared  $\alpha$ - $\text{Fe}_2\text{O}_3$  and  $\text{Fe}_3\text{O}_4$  nanorods both have a mesoporous structure, and it is thus expected that these single-crystalline mesoporous  $\alpha$ - $\text{Fe}_2\text{O}_3$  and  $\text{Fe}_3\text{O}_4$  nanorods may have improved electrochemical properties for lithium-ion battery applications.



**Fig. 7** (a) Charge–discharge profiles of single-crystalline mesoporous  $\alpha$ - $\text{Fe}_2\text{O}_3$  nanorod electrodes at different cycles in the potential range from 0.05 to 3.0 V with a low current density of 0.1 C; (b) cyclic voltammogram curves of single-crystalline mesoporous  $\alpha$ - $\text{Fe}_2\text{O}_3$  nanorod electrodes at a scan rate of 0.1  $\text{mV s}^{-1}$ ; (c) cycling performance and Coulombic efficiency of the cell at a 0.1 C rate; (d) the rate performance of the single-crystalline mesoporous  $\alpha$ - $\text{Fe}_2\text{O}_3$  nanorod electrode.

Fig. 7a reveals the charge–discharge profiles of the mesoporous  $\alpha$ - $\text{Fe}_2\text{O}_3$  nanorods at a low current density of 0.1 C rate in the voltage window of 0.05–3 V. There is a distinct voltage plateau at 0.85 V, corresponding to the reduction from  $\text{Fe}^{2+}$  to  $\text{Fe}^0$  and the formation of amorphous  $\text{Li}_2\text{O}$ .<sup>31</sup> The first discharge capacity of the  $\alpha$ - $\text{Fe}_2\text{O}_3$  nanorods is 1230.4  $\text{mA h g}^{-1}$ , which is much larger than the first charge capacity (955.8  $\text{mA h g}^{-1}$ ). The Coulombic efficiency is only 77.7% in the first cycle. This irreversible capacity loss of about 274.6  $\text{mA h g}^{-1}$  can be mainly attributed to the possible irreversible processes such as electrolyte decomposition and the inevitable formation of a solid electrolyte interface (SEI) layer.<sup>10,11,25,26,31</sup> In the second cycle, however, the Coulombic efficiency increases rapidly to 94%. The discharge and charge capacities of the 2<sup>nd</sup> cycle are 980.9 and 922.8  $\text{mA h g}^{-1}$ , respectively. Accompanied by the increased cycle number, the discharge capacity of the  $\alpha$ - $\text{Fe}_2\text{O}_3$  nanorods is 893.3  $\text{mA h g}^{-1}$  after the 50<sup>th</sup> cycle, and the Coulombic efficiency steadily reaches around 98%.

The detailed electrochemical behaviour of the  $\alpha$ - $\text{Fe}_2\text{O}_3$  nanorods was tested by CV tests (Fig. 7b). It can be found that there are two reduction peaks (1.62 and 0.71 V) in the first cathodic sweep, indicating the following two lithiation processes:<sup>25,26,31,32</sup> Firstly, a small amount of lithium can be inserted into the crystal structure of  $\alpha$ - $\text{Fe}_2\text{O}_3$ , followed by a transformation to cubic  $\text{Li}_2\text{Fe}_2\text{O}_3$  ( $\alpha\text{-Fe}_2\text{O}_3 + 2\text{Li}^+ + 2\text{e}^- \rightarrow \text{Li}_2\text{Fe}_2\text{O}_3$  (cubic)). In the second step,  $\text{Fe}^{2+}$  will be reduced to  $\text{Fe}^0$  completely and the electrolyte will decompose ( $\text{Li}_2\text{Fe}_2\text{O}_3$  (cubic) +  $4\text{Li}^+ + 4\text{e}^- \rightarrow 2\text{Fe} + 3\text{Li}_2\text{O}$ ). In the first anodic sweep, there are two small oxidation peaks at 1.68 and 1.86 V, corresponding to the oxidation of  $\text{Fe}^0$  to  $\text{Fe}^{2+}$  and  $\text{Fe}^{3+}$  to reform  $\text{Fe}_2\text{O}_3$ .<sup>31</sup> During the subsequent cycles, on the one hand, the initial two reduction peaks at 1.62 and 0.71 V disappear as a result of irreversible phase transitions from  $\alpha$ - $\text{Li}_x\text{Fe}_2\text{O}_3$  to cubic  $\text{Li}_2\text{Fe}_2\text{O}_3$  and SEI film formation. On the other hand, CV curves exhibit good reproducibility with a cathodic and anodic peak pair at 0.8 V and 1.6–1.8 V for reversible conversion between  $\text{Fe}^{2+}$  and  $\text{Fe}^0$ .

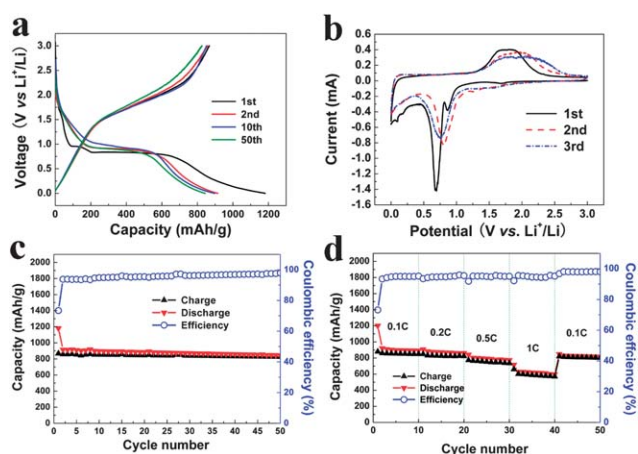
Fig. 7c and d display the long-time cycling performance and rate performance of the  $\alpha$ -Fe<sub>2</sub>O<sub>3</sub> nanorods. At a low rate of 0.1 C, from the second cycle onward, the  $\alpha$ -Fe<sub>2</sub>O<sub>3</sub> nanorods show fascinating cycling stability (Fig. 7c). After 50 cycles, the discharge and charge capacities are retained well, and the Coulombic efficiency is increased to 98%. The 50<sup>th</sup> discharge capacity is still higher than 893 mA h g<sup>-1</sup>, which corresponds to a 91% capacity retention of the 2<sup>nd</sup> discharge capacity of 980.9 mA h g<sup>-1</sup> and 89% of the theoretical capacity of 1004 mA h g<sup>-1</sup>. According to the rate capacity in Fig. 7d, the discharge capacity is slightly reduced to 980, 915, 820 mA h g<sup>-1</sup> at rates of 0.1 C, 0.2 C and 0.5 C, respectively. Even at a 1 C rate, the discharge capacity of the  $\alpha$ -Fe<sub>2</sub>O<sub>3</sub> electrode is still higher than 600 mA h g<sup>-1</sup>. It should be noted that as long as the current density reverses back to the initial rate of 0.1 C, the electrode can retain the original discharge capacity of 920 mA h g<sup>-1</sup>. Meanwhile, compared with similar works relating to mesoporous  $\alpha$ -Fe<sub>2</sub>O<sub>3</sub> nanorods, Cherian *et al.*<sup>10</sup> and Yao *et al.*<sup>11</sup> both proved that these improved electrochemical performances can be ascribed to the unique mesoporous microstructure.

Furthermore, to identify the effect of the mesoporous structure and the 1D nanorod morphology of Fe<sub>3</sub>O<sub>4</sub> on its electrochemical performance, the as-prepared single-crystalline mesoporous Fe<sub>3</sub>O<sub>4</sub> nanorods were also tested by a Fe<sub>3</sub>O<sub>4</sub>-Li half cell. The charge-discharge profiles of the Fe<sub>3</sub>O<sub>4</sub> nanorods are shown in Fig. 8a. As seen in Fig. 8a, the first discharge profile is similar to that of  $\alpha$ -Fe<sub>2</sub>O<sub>3</sub>. The step voltage range from 3 to 0.8 V refers to the formation of a Li-Fe-O compound.<sup>22</sup> The long voltage plateau at 0.8 V can be ascribed to the conversion reaction of the Li-Fe-O compound to Fe and Li<sub>2</sub>O.<sup>22,23</sup> The gradual voltage decay from 0.8 to 0.05 V corresponds to the formation of an SEI film and electrolyte decomposition.<sup>14,22,23</sup> The first charge and discharge capacities of the Fe<sub>3</sub>O<sub>4</sub> nanorods are 867.1 and 1181.5 mA h g<sup>-1</sup>, respectively. It has a large irreversible capacity (314.4 mA h g<sup>-1</sup>), which is caused by the conversion of Fe<sub>3</sub>O<sub>4</sub> to

Fe, along with the formation of amorphous Li<sub>2</sub>O and the SEI film.<sup>32-36</sup> From the second cycle onward, the well-defined potential plateaus at 0.8 and 1.6 V can be attributed to the reversible reduction-oxidation reactions between Fe<sub>3</sub>O<sub>4</sub> and Fe. The irreversible capacity decreases rapidly, and the Coulombic efficiency is increased. The CV curves of the as-prepared Fe<sub>3</sub>O<sub>4</sub> nanorods also clarify clearly the electrochemical reactions (Fig. 8b). In the first cathodic sweep, the peaks at 0.69 and 0.86 V represent the conversion of Fe<sub>3</sub>O<sub>4</sub> to Fe and the formation of amorphous Li<sub>2</sub>O (Fe<sub>3</sub>O<sub>4</sub> + 8Li<sup>+</sup> + 8e<sup>-</sup>  $\leftrightarrow$  3Fe + 4Li<sub>2</sub>O), as well as the irreversible reaction with the electrolyte.<sup>14,35,36</sup> Meanwhile, in the anodic process, a wide peak at 1.75 V is due to the reversible oxidation of Fe to Fe<sup>3+</sup>.<sup>14,36</sup> During the following two cycles, the reduction and oxidation peaks are both positively shifted, implying the polarization of the electrode at the first cycle. However, the subsequent cycles almost overlapped, indicating the good electrochemical reversibility of the single-crystalline mesoporous Fe<sub>3</sub>O<sub>4</sub> electrode.

The cyclic stability and rate performance of the single-crystalline mesoporous Fe<sub>3</sub>O<sub>4</sub> nanorods were also tested by long-term cycling at a low current density of 0.1 C and multi-rate cycling with different current densities. As shown in Fig. 8c, from the second cycle onward, the charge and discharge capacities of the Fe<sub>3</sub>O<sub>4</sub> electrode are retained well, and the Coulombic efficiency is steadily increased with increasing cycle number. After 50 cycles, the discharge and charge capacities of the Fe<sub>3</sub>O<sub>4</sub> electrode are 843.5 and 825.4 mA h g<sup>-1</sup>, respectively. Compared with the initial discharge capacity (914.9 mA h g<sup>-1</sup> for the 2<sup>nd</sup> cycle), the capacity retention is over 92%, indicating that the single-crystalline mesoporous Fe<sub>3</sub>O<sub>4</sub> nanorods have outstanding structural stability. When the current density is increased from 0.1 C to 1 C, the discharge and charge capacities remain stable and decrease regularly with an enhanced rate. The reversible capacities at 0.1, 0.2, 0.5 and 1 C rate are about 892.2, 861.7, 841.7 and 715.7 mA h g<sup>-1</sup>, which are 96.8, 94.9, 91.9 and 83.5% of the initial discharge capacities. After 40 cycles, the current rate is reduced to 0.1 C. The Fe<sub>3</sub>O<sub>4</sub> electrode still can deliver a reversible capacity of about 820 mA h g<sup>-1</sup>, which is 88.7% of the theoretical capacity of 924 mA h g<sup>-1</sup>. It is demonstrated that the mesoporous structure of the Fe<sub>3</sub>O<sub>4</sub>-C nanorods will play an important role in relieving the impact of volume changes during the repeated charge-discharge processes.<sup>22</sup> Therefore, these Fe<sub>3</sub>O<sub>4</sub> nanorods present remarkable cyclic stability and rate performance, probably due to the mesoporous structure.

Additionally, in order to evaluate the electrochemical dynamical behaviors of  $\alpha$ -FeOOH,  $\alpha$ -Fe<sub>2</sub>O<sub>3</sub> and Fe<sub>3</sub>O<sub>4</sub>, electrochemical impedance spectroscopy (EIS) measurements were performed. All the samples were measured at room temperature using fresh cells. As shown in Fig. 9, the EIS spectra of the  $\alpha$ -FeOOH,  $\alpha$ -Fe<sub>2</sub>O<sub>3</sub> and Fe<sub>3</sub>O<sub>4</sub> samples are composed of a quasi-semicircle in the range from high to middle frequency and a straight sloping line in the low frequency range. The inset shows an equivalent circuit model according to the simulation. The high frequency one can be attributed to the resistance ( $R_{\text{sei}}$ ) and capacitance ( $C_{\text{sei}}$ ) of the formation of the SEI film. The medium frequency one is associated with the charge-transfer resistance ( $R_{\text{ct}}$ ) and its double-layer capacitance (CPE). The sloped line at low frequency is related to the Warburg impedance ( $Z_{\text{w}}$ ) of the lithium ion diffusion. From the plots, it is

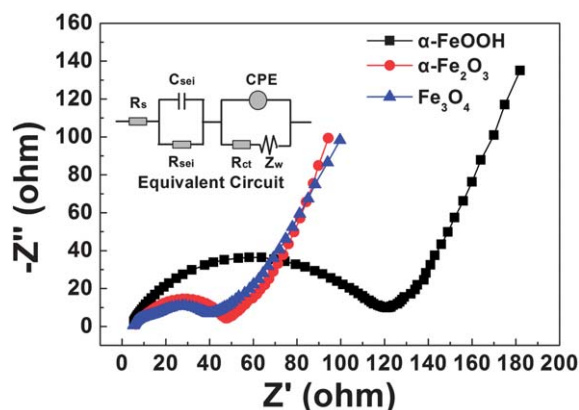


**Fig. 8** (a) Charge-discharge profiles of single-crystalline mesoporous Fe<sub>3</sub>O<sub>4</sub> nanorod electrodes at different cycles in the potential range from 0.05 to 3.0 V with a low current density of 0.1 C; (b) cyclic voltammogram curve of single-crystalline mesoporous Fe<sub>3</sub>O<sub>4</sub> nanorod electrodes at a scan rate of 0.1 mV s<sup>-1</sup>; (c) cycling performance and Coulombic efficiency of the cell at a 0.1 C rate; (d) the rate performance of single-crystalline mesoporous Fe<sub>3</sub>O<sub>4</sub> nanorod electrode.



**Table 1** The electrochemical performances of  $\alpha$ -FeOOH,  $\alpha$ -Fe<sub>2</sub>O<sub>3</sub> and Fe<sub>3</sub>O<sub>4</sub> samples

Sample	Theoretical capacity (mA h g <sup>-1</sup> )	Retention rate of long-term cycling at a 0.1 C rate	Multi-rate performance (mA h g <sup>-1</sup> )				Kinetic parameters ( $\Omega$ )		
			0.1 C	0.2 C	0.5 C	1 C	$R_s$	$R_{sei}$	$R_{ct}$
$\alpha$ -FeOOH	905	<25% (20 cycles)	542	210	145	54	6.3	17.6	100.9
$\alpha$ -Fe <sub>2</sub> O <sub>3</sub>	1004	91% (50 cycles)	980	915	820	600	5.5	17.2	27.7
Fe <sub>3</sub> O <sub>4</sub>	924	92% (50 cycles)	892	862	842	716	5.1	16.8	20.1

**Fig. 9** EIS spectra of  $\alpha$ -FeOOH,  $\alpha$ -Fe<sub>2</sub>O<sub>3</sub> and Fe<sub>3</sub>O<sub>4</sub> fresh cells in the frequency range of 0.1–10<sup>6</sup> Hz at room temperature. The inset is an equivalent circuit.

obvious that the radii of the quasi-semicircle of  $\alpha$ -Fe<sub>2</sub>O<sub>3</sub> and Fe<sub>3</sub>O<sub>4</sub> with a mesoporous structure are much smaller than that of  $\alpha$ -FeOOH without a mesoporous structure. The low  $R_{ct}$  is beneficial to enhance the electron kinetics in electrode materials.<sup>37,38</sup> On the basis of the equivalent circuit parameters, both mesoporous  $\alpha$ -Fe<sub>2</sub>O<sub>3</sub> and Fe<sub>3</sub>O<sub>4</sub> samples have low  $R_{ct}$  values, implying that the mesoporous structure can effectively improve the electron transport. Furthermore, after a careful comparison, it could be found that the Fe<sub>3</sub>O<sub>4</sub> sample has the smallest  $R_{ct}$ . This improvement of the Fe<sub>3</sub>O<sub>4</sub> sample with the smallest  $R_{ct}$  could be attributed to the trace amount of residual carbon (according to the TG results, the carbon content is about 5%) in the synthesis process. Therefore, the electron transport ability of Fe<sub>3</sub>O<sub>4</sub> is better than that of  $\alpha$ -Fe<sub>2</sub>O<sub>3</sub> although  $\alpha$ -Fe<sub>2</sub>O<sub>3</sub> and Fe<sub>3</sub>O<sub>4</sub> have a similar microstructure. In addition, the electrochemical data of the  $\alpha$ -FeOOH,  $\alpha$ -Fe<sub>2</sub>O<sub>3</sub> and Fe<sub>3</sub>O<sub>4</sub> samples have also been listed in Table 1 as a comparison. As shown in Table 1, it is clear that although the theoretical capacity of the mesoporous Fe<sub>3</sub>O<sub>4</sub> nanorods is lower than that of  $\alpha$ -Fe<sub>2</sub>O<sub>3</sub>, the electrochemical dynamic behavior and cycling performance are better than that of  $\alpha$ -Fe<sub>2</sub>O<sub>3</sub>.

Based on the above results, the single crystal  $\alpha$ -Fe<sub>2</sub>O<sub>3</sub> and Fe<sub>3</sub>O<sub>4</sub> electrodes with mesoporous structures compared with  $\alpha$ -FeOOH without a mesoporous structure have the following advantages for enhancing the electrochemical performance. On the one hand, the  $\alpha$ -Fe<sub>2</sub>O<sub>3</sub> and Fe<sub>3</sub>O<sub>4</sub> nanorods with mesoporous structures enhance the contact area between the electrode and electrolyte and allow better penetration of the electrolyte. On the other hand, mesoporous structures can accommodate the strain induced by the volume changes during repeated charge-discharge cycling processes.

## 4. Conclusions

In summary, single crystal mesoporous  $\alpha$ -Fe<sub>2</sub>O<sub>3</sub> and Fe<sub>3</sub>O<sub>4</sub> nanorods have been successfully prepared by calcining the corresponding  $\alpha$ -FeOOH precursor, while preserving their original morphologies. When tested as the anode materials for LIBs, the as-synthesized mesoporous  $\alpha$ -Fe<sub>2</sub>O<sub>3</sub> and Fe<sub>3</sub>O<sub>4</sub> nanorods demonstrated a very high reversible capacity of 893.3 mA h g<sup>-1</sup> and 843.5 mA h g<sup>-1</sup> after the 50<sup>th</sup> cycle at 0.1 C, respectively. These can be ascribed to the porous structure of the  $\alpha$ -Fe<sub>2</sub>O<sub>3</sub> and Fe<sub>3</sub>O<sub>4</sub> nanorods. This 1D mesoporous morphology could shorten pathways for lithium-ion diffusion, enhance the contact area between the electrode and electrolyte, and accommodate the strain induced by volume changes during the charge-discharge process. The electrochemical dynamic results also confirm the superior electron transport ability of single crystal mesoporous Fe<sub>3</sub>O<sub>4</sub> nanorods, making the Fe<sub>3</sub>O<sub>4</sub> nanorods highly attractive for potential application as an anode material in high energy and high power lithium-ion batteries. In addition, these low-cost mesoporous materials could also be desirable objects for applications in other fields, such as gas-sensors, magnetic materials, catalysis and hydrogen storage.

## Acknowledgements

This work was financially supported by the National Natural Science Foundation of China (Grant no. 51102212), Cyrus Tang Center for Sensor Materials and Applications (112205-M11201/005), the Fundamental Research Funds for the Central Universities (no. 588040\*172210221/014) and the Opening Foundation of Zhejiang Provincial Top Key Discipline.

## Notes and references

- X. L. Mou, B. S. Zhang, Y. Li, L. D. Yao, X. J. Wei, D. S. Su and W. J. Shen, *Angew. Chem., Int. Ed.*, 2012, **51**, 2989–2993.
- X. L. Hu and J. C. Yu, *Adv. Funct. Mater.*, 2008, **18**, 880–887.
- Y. F. Yu, J. Zhang, X. Wu, W. W. Zhao and B. Zhang, *Angew. Chem., Int. Ed.*, 2012, **51**, 897–900.
- L. Tian, H. L. Zou, J. X. Fu, X. F. Yang, Y. Wang, H. L. Guo, X. H. Fu, C. L. Liang, M. M. Wu, P. K. Shen and Q. M. Gao, *Adv. Funct. Mater.*, 2010, **20**, 617–623.
- C. J. Jia, L. D. Sun, Z. G. Yan, L. P. You, F. Luo, X. D. Han, Y. C. Pang, Z. Zhang and C. H. Yan, *Angew. Chem., Int. Ed.*, 2005, **44**, 4328–4333.
- Y. J. Xiong, Z. Q. Li, X. X. Li, B. Hu and Y. Xie, *Inorg. Chem.*, 2004, **43**, 6540–6542.
- J. Kong, N. R. Franklin, C. W. Zhou, M. G. Chapline, S. Peng, K. Cho and H. J. Dai, *Science*, 2000, **287**, 622–625.
- G. X. Wang, X. L. Gou, J. Horvat and J. Park, *J. Phys. Chem. C*, 2008, **112**, 15220–15225.
- S. J. Ding, J. S. Chen and X. W. Lou, *Adv. Funct. Mater.*, 2011, **21**, 4120–4125.
- C. T. Cherian, J. Sundaramurthy, M. Kalaivani, P. Ragupathy, P. S. Kumar, V. Thavasi, M. V. Reddy, C. H. Sow,

- S. G. Mhaisalkar, S. Ramakrishna and B. V. R. Chowdari, *J. Mater. Chem.*, 2012, **22**, 12198–12204.
- 11 X. Y. Yao, C. L. Tang, G. X. Yuan, P. Cui, X. X. Xu and Z. P. Liu, *Electrochem. Commun.*, 2011, **13**, 1439–1442.
  - 12 X. L. Hu, J. C. Yu, J. M. Gong, Q. Li and G. S. Li, *Adv. Mater.*, 2007, **19**, 2324–2329.
  - 13 F. Y. Cao, C. L. Chen, Q. Wang and Q. W. Chen, *Carbon*, 2007, **45**, 727–731.
  - 14 G. M. Zhou, D. W. Wang, F. Li, L. L. Zhang, N. Li, Z. S. Wu, L. Wen, G. Q. Lu and H. M. Cheng, *Chem. Mater.*, 2010, **22**, 5306–5313.
  - 15 R. Rajendran, R. Muralidharan, R. S. Gopalakrishnan, M. Chellamuthu, S. U. Ponnusamy and E. Manikandan, *Eur. J. Inorg. Chem.*, 2011, 5384–5389.
  - 16 Z. S. Wu, W. C. Ren, L. Wen, L. B. Gao, J. P. Zhao, Z. P. Chen, G. M. Zhou, F. Li and H. M. Cheng, *ACS Nano*, 2010, **4**, 3187–3194.
  - 17 B. Varghese, M. V. Reddy, Y. W. Zhu, S. L. Chang, C. H. Teo, G. V. Subba Rao, B. V. R. Chowdari, A. T. S. Wee, C. T. Lim and C. H. Sow, *Chem. Mater.*, 2008, **20**, 3360–3367.
  - 18 G. M. Zhou, D. W. Wang, L. C. Yin, N. Li, F. Li and H. M. Cheng, *ACS Nano*, 2012, **6**, 3214–3223.
  - 19 Y. Xia, W. K. Zhang, Z. Xiao, H. Huang, H. J. Zeng, X. R. Chen, F. Chen, Y. P. Gan and X. Y. Tao, *J. Mater. Chem.*, 2012, **22**, 9209–9215.
  - 20 Z. Y. Wang, Z. C. Wang, S. Madhavi and X. W. Lou, *J. Mater. Chem.*, 2012, **22**, 2526–2531.
  - 21 J. S. Chen, T. Zhu, X. H. Yang, H. G. Yang and X. W. Lou, *J. Am. Chem. Soc.*, 2010, **132**, 13162–13164.
  - 22 S. M. Yuan, J. X. Li, L. T. Yang, L. W. Su, L. Liu and Z. Zhou, *ACS Appl. Mater. Interfaces*, 2011, **3**, 705–709.
  - 23 T. Yoon, C. Chae, Y. K. Sun, X. Zhao, H. H. Kung and J. K. Lee, *J. Mater. Chem.*, 2011, **21**, 17325–17330.
  - 24 J. S. Hu, L. S. Zhong, W. G. Song and L. J. Wan, *Adv. Mater.*, 2008, **20**, 2977–2982.
  - 25 Z. Y. Wang, D. Y. Luan, S. Madhavi, Y. Hu and X. W. Lou, *Energy Environ. Sci.*, 2012, **5**, 5252–5256.
  - 26 W. Zhou, L. J. Lin, W. J. Wang, L. L. Zhang, Q. Wu, J. H. Li and L. Guo, *J. Phys. Chem. C*, 2011, **115**, 7126–7133.
  - 27 C. M. Zhang, J. X. Zhu, X. H. Rui, J. Chen, D. H. Sim, W. H. Shi, H. H. Hng, T. M. Lim and Q. Y. Yan, *CrystEngComm*, 2012, **14**, 147–153.
  - 28 X. M. Lou, X. Z. Wu and Y. X. Zhang, *Electrochem. Commun.*, 2009, **11**, 1696–1699.
  - 29 S. Xiong, J. Xu, D. Chen, R. M. Wang, X. L. Hu, G. Z. Shen and Z. L. Wang, *CrystEngComm*, 2011, **13**, 7114–7120.
  - 30 Y. X. Chen, L. H. He, P. J. Shang, Q. L. Tang, Z. Q. Liu, H. B. Liu and L. P. Zhou, *J. Mater. Sci. Technol.*, 2011, **27**, 41–45.
  - 31 D. W. Su, H. S. Kim, W. S. Kim and G. X. Wang, *Microporous Mesoporous Mater.*, 2012, **149**, 36–45.
  - 32 S. M. Yuan, Z. Zhou and G. Li, *CrystEngComm*, 2011, **13**, 4709–4713.
  - 33 L. W. Ji, Z. K. Tan, T. R. Kuykendall, S. Aloni, S. D. Xun, E. Lin, V. Battaglia and Y. G. Zhang, *Phys. Chem. Chem. Phys.*, 2011, **13**, 7170–7177.
  - 34 J. Liu, Y. C. Zhou, F. Liu, J. B. Wang, Y. Pan and D. F. Xue, *RSC Adv.*, 2012, **2**, 2262–2265.
  - 35 S. K. Behera, *J. Power Sources*, 2011, **19**, 8669–8674.
  - 36 J. Z. Wang, C. Zhong, D. Wexler, N. H. Idris, Z. X. Wang, L. Q. Chen and H. K. Liu, *Chem.–Eur. J.*, 2011, **17**, 661–667.
  - 37 M. Zhang, B. H. Qu, D. N. Lei, Y. J. Chen, X. Z. Yu, L. B. Chen, Q. H. Li, Y. G. Wang and T. H. Wang, *J. Mater. Chem.*, 2012, **22**, 3868–3874.
  - 38 Y. Ma, C. Zhang, G. Ji and J. Y. Lee, *J. Mater. Chem.*, 2012, **22**, 7845–7850.